A Photoactive Ag(I) Based Coordination Polymer as a Potential Semiconductor for Photocatalytic Water Splitting and Environmental Remediation: Experimental and Theoretical Approach

Subrata Mandal[1], Sachin P. Nanavati[2], David J. Willock[2] and Rajakumar Ananthakrishnan[1]*

[1]Department of Chemistry, Environmental Materials & Analytical Chemistry Laboratory, Indian Institute of Technology, Kharagpur 721302, India
E-mail: raja.iitchem@yahoo.com; Fax: +91 3222-282252; Tel: +91 3222 282322

[2]Cardiff Catalysis Institute, School of Chemistry, Cardiff University, Cardiff, CF10 3AT, UK.

ABSTRACT Metal organic frameworks (MOFs) or Metal coordination polymers (CPs) with controlled structure on the micro/nano-scale have attracted intense interest for potential applications in a wide variety of fields, such as energy storage and conversion, chemical and biological sensing, and catalysis. Here, we report a new class of photocatalytic material, Ag(I) based nano-micro structured coordination polymer (Ag(I)-CP), which offer performance at a level competitive with known semiconductors in photocatalytic water oxidation and oxidation of organic compounds, such as dye/ organic pollutants present in contaminated water. The coordination polymer was synthesized by a wet-chemical route and has been characterized using powder X-ray diffraction, X-ray photoelectron spectroscopy and electron microscopy. The

21   Ag(I)-CP has notable semiconducting characteristics and charge transfer ability due to ligand

22   centered charge transfer (LCCT) in combination with metal to ligand charge transfer MLCT

23   (Ag-O cluster to ligand centre) as established from experimental absorption, luminescence and

24   photoelectrochemical measurements alongside DFT calculations. Notably, Ag(I)-CP exhibits a

25   highly reactive valance band potential +3.40 V *vs* NHE, composed of hybridized state of O *2p*

26   and C *2p* through the organic linker and Ag *4d*, this acts as an active center for the generation of

27   reactive oxygen species (ROS) *i.e.,* hydroxyl radical and h^+ under photocatalytic conditions.

28   Consequently, the photogenerated species facilitate effective oxidations of water and organic

29   contaminants such as tartrazine, rhodamine B and 2, 4-dichlorophenol under UV light

30   irradiation. Furthermore, our results suggest that the Ag(I)-CP could be used as a promising

31   material for the development of heterostructure for variety of photo-assisted-redox catalysis.

32   **INTRODUCTION**

33   Photocatalysis finds important applications for the oxidation of organic pollutants in industrial

34   water streams and for solar-energy conversion via water splitting. The pioneering work of

35   Fujishima and Honda on TiO2 in 1972, led researchers engaged in the applications of

36   semiconductor materials, such as TiO2, ZnO, CdS, *etc*. to turn to the field of photocatalysis.[1, 2]

37   However, such classical semiconductor based materials are not suited to large-scale application

38   in photocatalysis due to poor efficiencies resulting from limited surface area (low surface to

39   volume ratios), short life time of the charge carriers and low charge conductivity. Hence,

40   developing a new-generation heterogeneous photocatalysts became an important research task.

41   Recently, metal coordination polymer (CPs)/ metal organic frameworks (MOFs) have offered

42   new material design options to engineer structural and electronic properties in a flexible manner.

43　These materials have intriguing features such as uniform porous structures and tunable

44　functionalities. MOFs are crystalline solids are built up from metal-oxide clusters interconnected

45　by organic linkers and so provide a suitable platform for host-guest interactions.[3,4]Unlike

46　classical semiconductors, charge transport phenomenon and the separation of active h^+/e^- in

47　MOFs/CPs is greatly influenced by two discrete components (inorganic nodes and organic

48　linkers) which offers the opportunity to tune the material properties.[5] In particular, the work of

49　Garcia $et\ al.$[6] and Férey $et\ al.$[7] on photoactive MOF-5 and MIL-125(Ti), respectively, revealed

50　that these new-classes of semiconductor could be used in the field of photovoltaics/

51　photocatalysis. A sub-field of research has thus emerged with the aim of synthesizing new

52　MOF/CP based semiconductor materials with tuned optical response produced by modifying the

53　inorganic unit or the organic linker (length and chemical functionalization) through either

54　synthetic and/or computational screening programmes.[8,9]Although interesting properties have

55　been obtained the basic understanding of how the material composition and structure brings

56　about the optical and semiconducting behavior is still a matter of debate. For example, the charge

57　transfer process of MOF-5 is still controversial as Qiu $et\ al.$ revealed it is LLCT[10] rather than

58　LMCT[6] using relativistic density functional theory and time dependent DFT. So far, then,

59　understanding of the mechanism of the charge separation process and semiconducting behavior

60　of the MOF/CPs is at a relatively early stage. Hence, designing a new class of CPs/MOFs and

61　investigating their band structure with respect to change of metal nodes by a combined

62　experimental and computational approach would help to develop a more reliable understanding

63　of the origin of photocatalytic properties.[9, 11]Notably, CPs containing Ag(I) can give a versatile

64　class of materials distinct from transition metal-based materials through the characteristic

65　features of the Ag(I) cation, such as coordination adaptability and metal-metal interaction.[12,

66 [13]Usually, Ag(I) based semiconductors such as Ag_2O, Ag_3PO_4, Ag_3AsO_4, *etc.* are found to be

67 effective in photocatalysis.[14, 15, 16] However, their low-lying hybridized *5s-5s* states and/or *5s/5p-*

68 *4d* states of silver in the conduction band minimum (CBM) facilitate the reduction of lattice Ag^+

69 resulting in a high level of photo-leaching.[14, 15] Additionally, low surface area and stability,

70 prevent large-scale use of these simple compounds for photocatalytic applications.[14,17]

71 CPs/MOFs of Ag(I) with suitable organic linkers can provide an alternative strategy to design

72 highly active photocatalytic materials. Ag(I)-CPs can be formed using 1, 4-benzene dicarboxylic

73 acid (H_2bdc) as linker. H_2bdc takes on a bidentate coordination mode in Ag(I)-CP, which should

74 lead to improved stability of the Ag(I) species and so this approach has been used in our research

75 to synthesize a Ag(I)-CP material and to investigate its photochemical properties.

76 Herein we describe the synthesis of a nano-micro structured Ag(I) coordination polymer

77 (Ag(I)-CP) using a H_2bdc linker and experiments to explore the application of Ag(I)-CP as a new

78 class of photocatalytic material for the oxidation of organic contaminants such as tartrazine,

79 rhodamine B, and 2, 4 dichlorophenol in water. Detail investigation of the photochemical and

80 photophysical properties of the Ag(I)-CP in combination with electronic structure calculated by

81 density functional theory suggests that Ag(I)-CP exhibits semiconducting behavior and

82 undergoes a ligand centered (LCCT) accompanied with metal to ligand (MLCT) charge transfer

83 process. We find that a highly reactive hole with a potential +3.40 V vs NHE is generated after

84 excitation in UV light and propose that either the hole itself, or hydroxyl radicals generated when

85 this hole interacts with water, are responsible for the observed high photocatalytic activity.

86 Noteworthy, our Ag(I)-CP photocatalyst is capable to oxidize tartrazine under simulated sunlight

87 due to its UV active catalytic behavior in combination with sensitization of tartrazine from

88 visible light region.

EXPERIMENTAL SECTION

Chemicals and materials

1, 4-benzenedicarboxylic acid (H_2bdc) was obtained from Central Drug House (P) Ltd. (India). Silver nitrate was obtained from Sigma Aldrich. All other chemical reagents utilized in the present work were analytical grade, purchased from Merck Specialties Private Limited and used without further purification. Deionized water was used throughout.

Synthesis of Ag(I)-CP

Ag(I)-CP was synthesized using the required stoichiometric amount of the precursor. In brief, 2 mmol of $AgNO_3$ was mixed in 10 mL aqueous ammonia solution (10 M) and stirred for 1 h, a transparent solution formed following reaction (1). Meanwhile, 1 mmol of H_2bdc was dissolved in 15 mL of water to form an aqueous solution to which 0.2 mL of 25% NH_3 was added. The dissolved H_2bdc was combined with the $AgNO_3$ solution and the resulting mixture was continuously stirred for 2 h before the final solid product, Ag(I)-CP produced following reaction (2), could be collected by centrifugation. The product was washed with deionized water and ethanol several times. The recovered solid powder was dried in an oven at 60° C for 12 h.

$$AgNO_3 + 2NH_4OH \rightarrow [Ag(NH_3)_2]^+ + NO_3^- + 2H_2O \tag{1}$$

$$[Ag(NH_3)_2]^+ + H_2bdc \rightarrow \quad Ag(I)\text{-}CP\downarrow + 2NH_4^+ \tag{2}$$
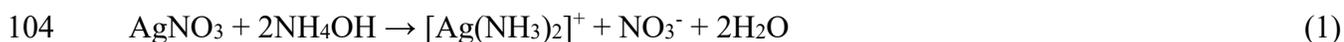
Synthesis of Ag_2O, CuO, TiO_2 and ZnO

To allow comparison of the photocatalytic activity of Ag(I)-CP with well-known light active semiconductors Ag_2O, CuO, TiO_2, ZnO materials were prepared following literature reported procedures[18, 19, 20] and further characterized by powder X-ray diffraction pattern as shown in Figure S4a.

Characterizations

The Fourier Transform Infra-Red spectrum of the Ag(I)-CP was recorded with a Perkin-Elmer FT-IR spectrophotometer RXI. The X-ray diffraction (XRD) pattern of Ag(I)-CP was obtained using a BRUKER-AXS-D8-ADVANCE diffractometer with Cu Kα radiation ($\lambda = 1.5418$ Å) in the 2θ range 5°-90° at a scan rate of 0.5° min^{-1}. X-ray Photoelectron Spectroscopy (XPS) was performed by Specs (Germany) to investigate the surface atomic composition and oxidation state of the elements present in the Ag(I)-CP. Electron Microscopy (FESEM) is used for morphological characterization of the Ag(I)-CP using a microscope accelerating voltage of 5 kV (NOVA NANOSEM 450). TEM images were obtained by JEOL JEM-2100 transmission electron microscopes, elemental mapping and dark field imaging is done in STEM mode with HAADF detector. TEM Samples were prepared by dropping a few samples dispersed in ethanol on carbon-coated 200 mesh copper grids. BET surface area and N_2 sorption isotherms (77K) of the prepared Ag(I)-CP was carried out by using Micromeritics ASAP 2020. For adsorption-desorption study the sample was degassed overnight and 50 mg was loaded in a 6 mm sample holder. Brunauer–Emmett–Teller (BET) calculations are performed for the analysis of surface area of the sample. UV–Vis diffuse reflectance spectra (UV–Vis DRS) were obtained by a Cary 500 UV–Vis spectrophotometer using $BaSO_4$ powder as an internal standard. Photoluminescence emission and excitation spectra of the prepared Ag(I)-CP and ligand were recorded by Horiba fluorolog-3 (solid state). In addition Ag(I)-CP sample before and after use in photocatalytic process were excited at 325 nm to investigate the change in recombination rate of hole and electron upon light irradiation.

Photoelectrochemical measurements

An electrochemical station is used to measure photocurrent using a three-electrode mode with 0.5 M Na_2SO_4 solution (pH = 7.0) as the electrolyte. In brief, 10 mg of Ag(I)-CP was added to 1

135   mL of ethanol. The as-prepared solution was stirred for 30 min to ensure that the Ag(I)-CP was

136   uniformly dispersed in the solution. 10 μL of the 10 mg mL^{-1} Ag(I)-CP solution was dropped on

137   to the surface of Fluorine doped Tin Oxide (FTO) substrate, which had an exposed area of 1.5 ×

138   1.3 cm^2, and then dried under vacuum conditions for 1 h at 60 °C. This step was repeated five

139   times to get uniform exposure of Ag(I)-CP on FTO. The resulting Ag(I)-CP photo anodes were

140   used as working electrodes; a Pt wire was used as a counter electrode. The Ag/AgCl electrode

141   was chosen as the reference electrodes. A 300 W-@ 1 Sun light intensity Xe lamp was used as

142   the light source (Solar simulator: Bat Sol). The Mott–Schottky measurements were performed at

143   frequency of 200-2000 Hz in the dark.

144   **Computational method**

145   The electronic structure of Ag(I)-CP was obtained using density functional theory (DFT) as

146   implemented in Vienna *Ab initio* Simulation Package (VASP).[21,22] The interaction between the

147   valence electrons and the core nuclei was approximated with the projector augmented wave

148   (PAW) pseudopotential method.[23] In the calculations the valence electrons are expanded in terms

149   of plane wave basis sets with an energy cutoff (E$_{cut}$) of 400 eV. The valence electronic

150   configuration of the constituent atoms are as follows: Ag: [Kr] $4d^{10}$ $5s^1$, O: [He] $2s^2$ $2p^4$, C: [He]

151    $2s^2$ $2p^2$ and H: $1s^1$. The Generalized Gradient Approximation (GGA) as parameterized by

152   Perdew-Burke-Ernzerhof (PBE)[24] was used to calculate the exchange-correlation energy. GGA

153   generally underestimates the band gap of a semiconductor and so, for better comparison with the

154   experimental data, the band structure was also generated using HSE06 hybrid functional[25, 26] with

155   a setting of 25% for the contribution from the short ranged Hartree-Fock exact exchange energy.

156   The initial structure of the Ag(I) based polymer was taken from single crystal X-ray diffraction

157   data (CCDC 198096). The unit cell of the Ag(I)-CP is composed of a simple monoclinic cell

158   with a total number of 36 atoms with composition $Ag_4C_{16}H_8O_8$, the structure is shown in Figure

159   S18. The convergence criteria for energy and forces are taken to be ~ 10^{-5} eV and ~ 0.005 eVÅ^{-1},

160   respectively. The Brillouin Zone (BZ) is sampled by a mesh of 3×3×3 k-points generated by

161   Monkhorst-Pack method.[27] The electronic structure has been smeared with a Gaussian of

162   standard deviation 0.1 eV. The electronic band structure is generated after sampling the first BZ

163   along high symmetry path Γ (G)—Z—D—B—Γ (G)—A—E—Z—C2—Y2—Γ (G), according

164   to the recipe provided by Hinuma *et al*.[28] To estimate atomic charges Bader topological

165   analysis[29, 30, 31] was employed.

166   In the Bader charge (BC) analysis, a surface is used to define the Bader region surrounding

167   each atom of a compound from which charge density is assigned to that atom. The surface runs

168   through the minima of the charge density in the location of the atom and the total charge for each

169   atom is determined by integration of the electron density within the Bader region. The calculated

170   Bader charges for the Ag(I)-CP are given in Table S1.

171   **Evaluation of photocatalytic activity**

172   Study on the water oxidation:

173   20 mg of the Ag(I)-CP catalyst and 10 mL of 0.01 M $AgNO_3$ *aq.* were loaded into a 50 mL two

174   necked Pyrex glass vessel containing Ar. The resulting mixture was irradiated with UV light

175   from a source of 250 W Hg lamps with gentle stirring. Hg lamp covers entire UV region (Xe

176   lamp emits selective lines in UV region) and hence the Hg lamp was chosen for the entire

177   photocatalytic process. The gaseous product (10 mL) was collected using an airtight syringe of

178   50 mL volume and analyzed by a GC (Thermo Fisher Scientific GC-Trace 1110) equipped with

179   a TCD detector and a molecular sieve 5Å packed column. The reaction was also carried out

180   without illumination (dark) keeping other experimental conditions unchanged.

181   The photocatalytic oxidation of Tartrazine, RhB and 2,4 DCP were studied using the following

182   methodology:

183   20 mg of the prepared catalyst was placed in a one necked Pyrex glass vessel (30 mL) with

184   mouth opened, which was then placed inside a photo reactor setup (an indigenously designed

185   reactor by Lelesil Innovative System, India), maintained at a distance of 25 cm from the light

186   source (250 W Hg lamp). Before light irradiation, the reaction vessel was placed in the dark and

187   stirred for 30 minutes to allow the adsorption-desorption equilibrium between the pollutants (20

188   mL of 25 ppm) and Ag(I)-CP (1 mg/mL) to be established, thereafter the light was turned-on.

189   During the progress of the reaction, 3 mL aliquots were collected at regular time intervals and

190   centrifuged to remove the catalyst. The aliquots of tartrazine and 2,4 DCP were characterized by

191   HPLC (Thermo Fisher Dionex UltiMate 3000 SD) using a diode array detector set to a

192   wavelength of 452 nm for tartrazine and 284 nm for 2,4 DCP. The aliquots of tartrazine and RhB

193   were also investigated separately using UV-Visible absorption spectroscopy (Thermo Scientific

194   Evolution 201 UV−vis spectrophotometer). The degradation percentages for all the experiments

195   are calculated using expression (1):

196   Degradation (%) = $(C_0 - C_t)/C_0 \times 100\%$ (1)

197   Where C_0 and C_t are the concentration of the aliquots illuminated for 0 and t min, respectively.

198   For comparison a study of the degradation of tartrazine was carried out using prepared

199   semiconductor materials including Ag_2O, TiO_2, ZnO, and CuO by keeping other experimental

200   conditions as similar.

201   **Gas and Ion Chromatographic Details**

202   The gaseous product (10 mL) from the degradation of tartrazine was collected by airtight

203   syringe (50 mL) and analyzed by a GC (Thermo Fisher Scientific GC-Trace 1110) equipped with

204   a FID detector and a molecular sieve 5Å packed column.

205   The ions present in the aqueous phase after photocatalysis (for degradation of tartrazine) were

206   analyzed by an ion chromatograph (Thermo Fisher, Dionex ICS-2100 connected with a Software

207   Chromeleon 7) equipped with Anion column- AS11, KOH as an eluent, using a run time of 12

208   min and Cation column - CS17, Methane Sulphonic Acid (MSA) as an eluent, using a run time

209   of 20 min.

210   The GC-MS (Thermo Scientific Trace 1300 Gas Chromatography and ISQ single Quadrupole

211   MS) and the LC-MS (Agilent 1200 infinity series LC and 6120 single quadrupole MS) of the

212   product in the degradation of tartrazine in different time interval was carried out, the reaction

213   mixture was first filtered to separate out the catalyst, then the remaining filtrate was extracted in

214   ethyl acetate and filtered over anhydrous Na_2SO_4 to absorb water molecules. The organic solvent

215   (EtOAc) was evaporated to dryness by a rotary evaporator. The dried product was dissolved in a

216   minimum amount of acetonitrile, and analyzed by GC-MS and LC-MS.

217

218   **RESULTS AND DISCUSSION**

219   We accessed a facile precipitation route to synthesize nano-microstructure Ag(I) based

220   coordination polymers with the spacer H_2bdc. Initially, possible binding modes of the

221   organic linker bdc^{2-} to Ag^+ were evident from the FTIR spectra as shown in Figure S1a

222   and it has been clear that the characteristic C=O stretching frequency was lowered from

223   1692 cm^{-1} (for free ligand) to 1580 cm^{-1} when carboxylate oxygen atoms are taking part in

224   the coordination to the metal centre.[32] From the PXRD pattern (Figure 1a) of the prepared

225 sample, it was evident that the organic linker formed a binuclear species with the Ag(I) cation to

226 give a monoclinic structure as the diffraction pattern of the sample is well indexed with the

227 calculated pattern of binuclear Ag_2bdc species (CCDC 198096)[33].
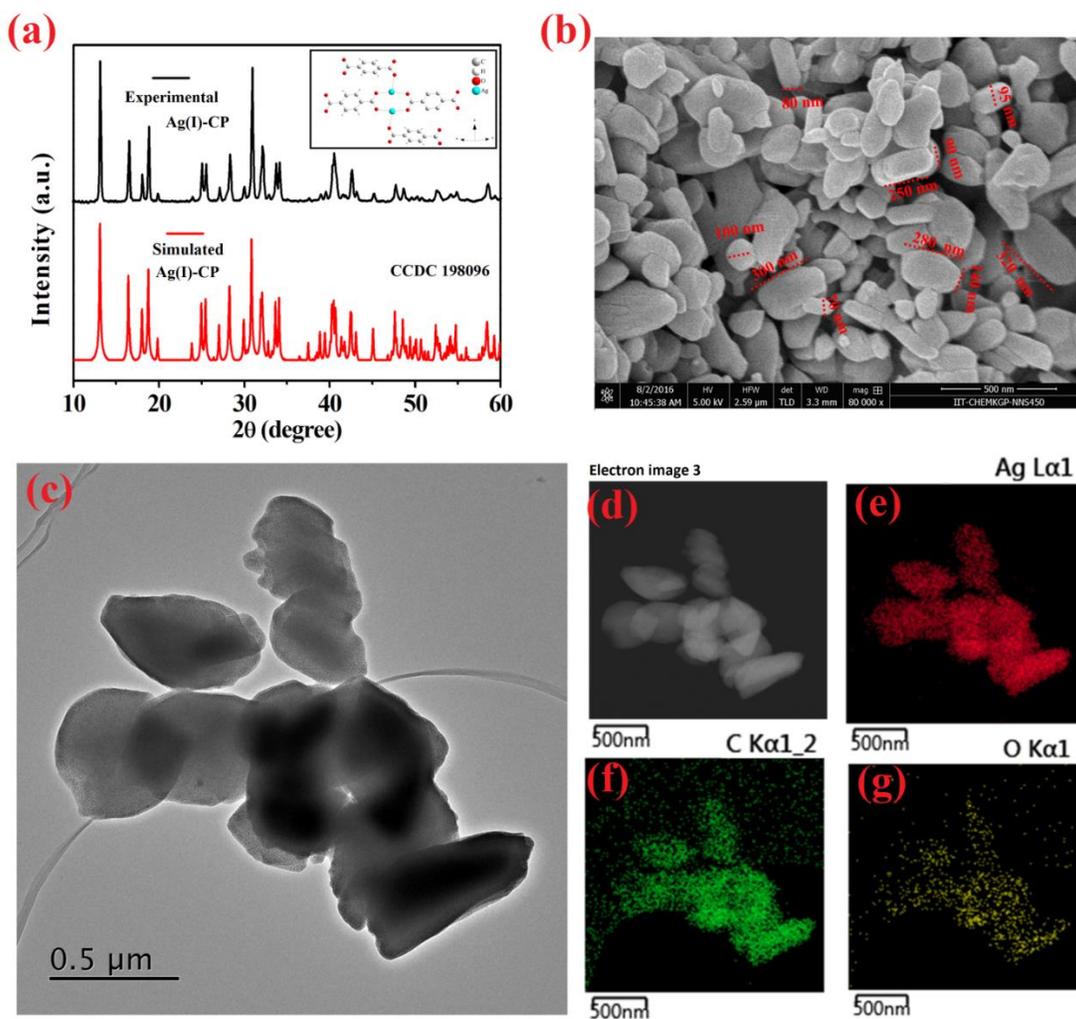
Figure 1. (a) PXRD pattern of prepared and simulated Ag(I)-CP (local structure of the CP shown in the inset) and (b) FESEM image, (c) TEM image of Ag(I)-CP with (d) STEM images and corresponding elemental mapping of (e) Ag, (f) C and (g) O.

228 No other phases of Ag(I) such as Ag_2O, Ag^0 are identified in the XRD pattern as verified from

229 the comparison of characteristics XRD pattern of Ag_2O (JCPDS No: 41-1104), Ag^0 (JCPDS No:

230 04-0783) (Figure S1b). The detailed structure further reveals that, Ag(I) is coordinated with T-

231 shaped geometry to the carboxylate oxygen atoms of the linker and that 1D chains are formed

232 from the species through sharing bdc^{2-} ligands in a head-to-tail fashion, whereas each 1 D chain

233 is connected others by weak Ag-O bonds, forming a 2D wave-like layer. The layers are

234 connected to each other by Ag–O bonds of the other linker carboxylate μ^2–O of bdc^{2-} and form a

235 3D framework (Figure S2a and Figure S2b). In addition, an Ag-Ag interaction occurs in the 3D

236 framework with a Ag-Ag distance of 2.9 Å (Figure S3b), which is significantly shorter than the

237 Ag-Ag Van der Waals contact distance (3.40 Å).[33] Field Emission Scanning Electron

238 Microscopic (FESEM) image (Figure 1b) and Transmission Electronic Microscopic (TEM)

239 image (Figure 1c) showed that the aqueous precipitation process used to prepare these samples

240 gives nano to micro size Ag(I)-CP. Further from elemental mapping profile it is obvious that

241 uniform distribution of Ag, O, and C in the structure of CP (Figure 1d-1g). BET measurements

242 give a moderate surface area of 39 m^2g^{-1} for the Ag(I)-CP materials and indicate a uniform pore

243 size with average pore diameter of ~ 8.9 nm (Figure S4b). The chemical state of the elements

244 present in the CP was verified using the XPS spectra shown in Figure 2a. The elements present

245 in the CP are Ag, O, and C. The high resolution XPS spectra of Ag($3d$) are shown in Figure 2b,

246 and show the binding energies of $3d_{5/2}$ and Ag $3d_{3/2}$ states in these samples are 367.1 eV and

247 373.1 eV respectively, which is in good agreement with the literature values for Ag in the +1

248 oxidation sate.[17] The presence of the organic spacer in the sample was confirmed by binding

249 energies of C-C (283.5 eV), C-O (285.0 eV), and C=C/C=O (286.9 eV) groups in the C $1s$

250 (Figure 2c).[34, 35]
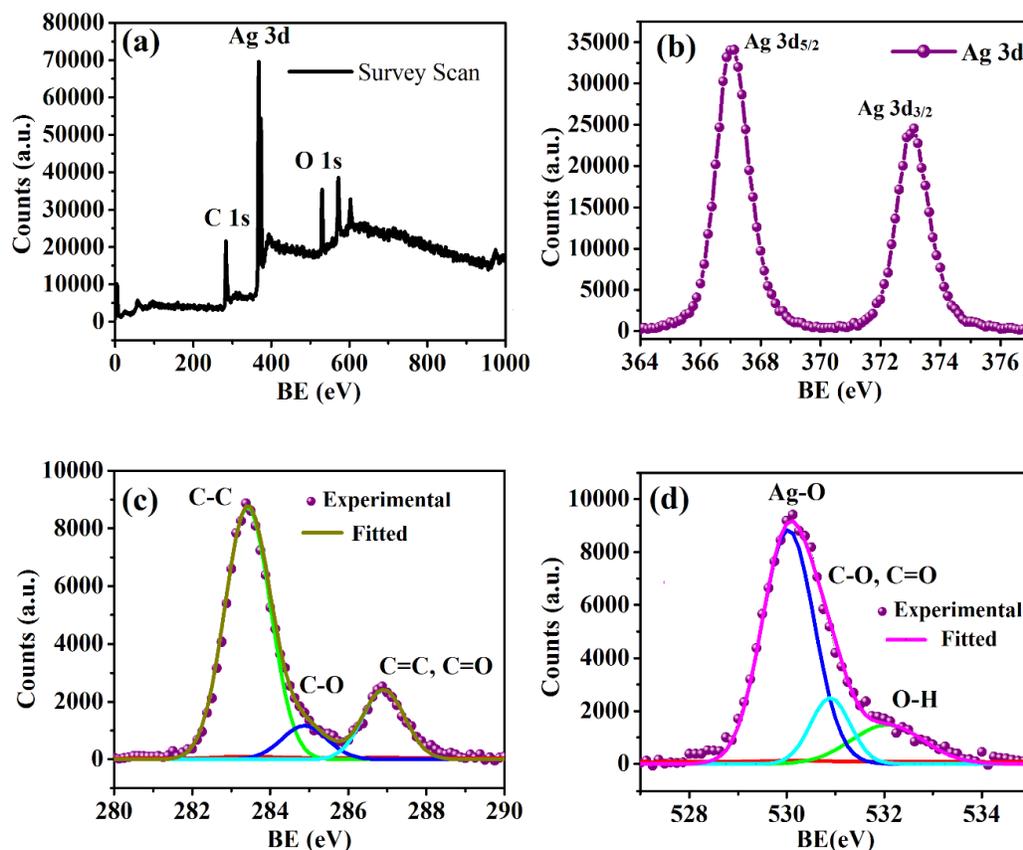
Figure 2. XPS spectra of surface elements of the prepared Ag(I)-CP: (a) Survey spectrum, (b) Ag element, (c) C element, (d) O element of Ag(I)-CP.

251   Solid state UV-visible absorption spectra of the free ligand H_2bdc and Ag(I)-CP were obtained

252   and are shown in Figure 3a. Both show strong absorption in the wavelength range of 200 - 360

253   nm. However, the absorption of the free ligand in the region of 200-360 nm illustrate the

254   feature of n→π* and π→π* transitions.[36] A hypsochromic shift of λ_{max} (~325 nm) assigned

255   as a ligand centred transition was observed in the Ag(I)-CP due to loss of co-planarity of the

256   phenyl ring and carboxylic moiety resulting from Ag-O bonding, as evidenced by the observed

257   dihedral angle of ~ 22-23° for C3- C2- C1- O2 and O1-C1-C2-C4 (Figure S3a). In addition, a

258   new weak shoulder peak located at 380 nm appeared in the low-energy region of the spectrum.

259 The Ag(I)-CP exhibits strong luminescence (Figure 3b) in the green region under irradiation by

260 UV light which can be seen by the naked eye both in solid state and when the material is

261 dispersed in water (Figure 3c). A solid-state luminescence study was carried out for the free

262 ligand ($\lambda_{ex} \sim 330$ nm) and for the Ag(I)-CP material ($\lambda_{ex} \sim 325$ nm).
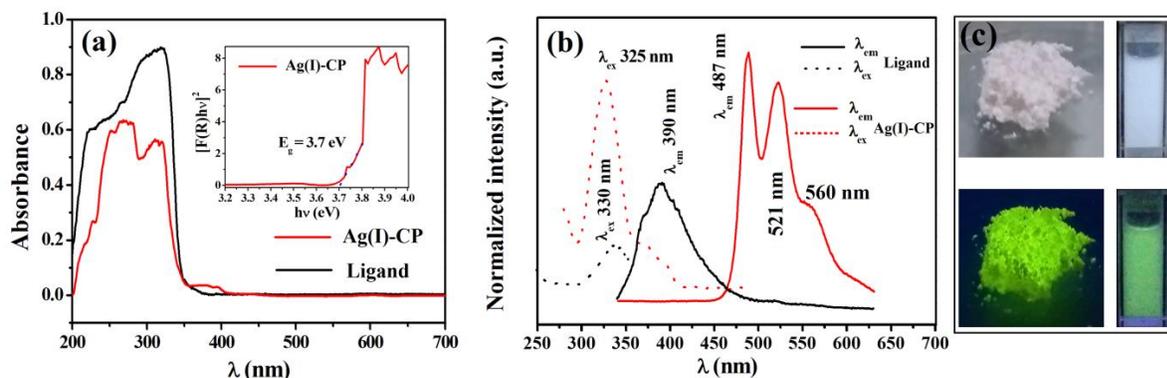
Figure 3. (a) UV-visible absorption spectra of free ligand (H$_2$bdc) and Ag(I)-CP (inset showing Kubelka-Munk plot for the CP), (b) photoluminescence spectra of free ligand (H$_2$bdc) and Ag(I)-CP upon excitation ($\lambda_{ex}\sim325$ nm for CP and $\lambda_{ex}\sim330$ nm for H$_2$bdc), and (c) photographs of the CP in solid state (left) and in aqueous dispersion (right) under daylight (above) and UV light (below).

263 Emission and excitation spectra of the free ligand and Ag(I)-CP are shown in Figure 3b, which

264 shows a weak ligand centered emission ($\pi^* \rightarrow \pi$ transition) at 390 nm ($\lambda_{ex} \sim 330$ nm) in H$_2$bdc,[36]

265 for Ag(I)-CP an intense radiative emission in the region of 460-600 nm ($\lambda_{ex} \sim 325$ nm) is

266 observed. The emission in the higher wavelength region (460-600 nm) is expected due to a

267 MLCT transition modified by metal-centered (d-s) states having Ag–Ag interactions.[37, 38]
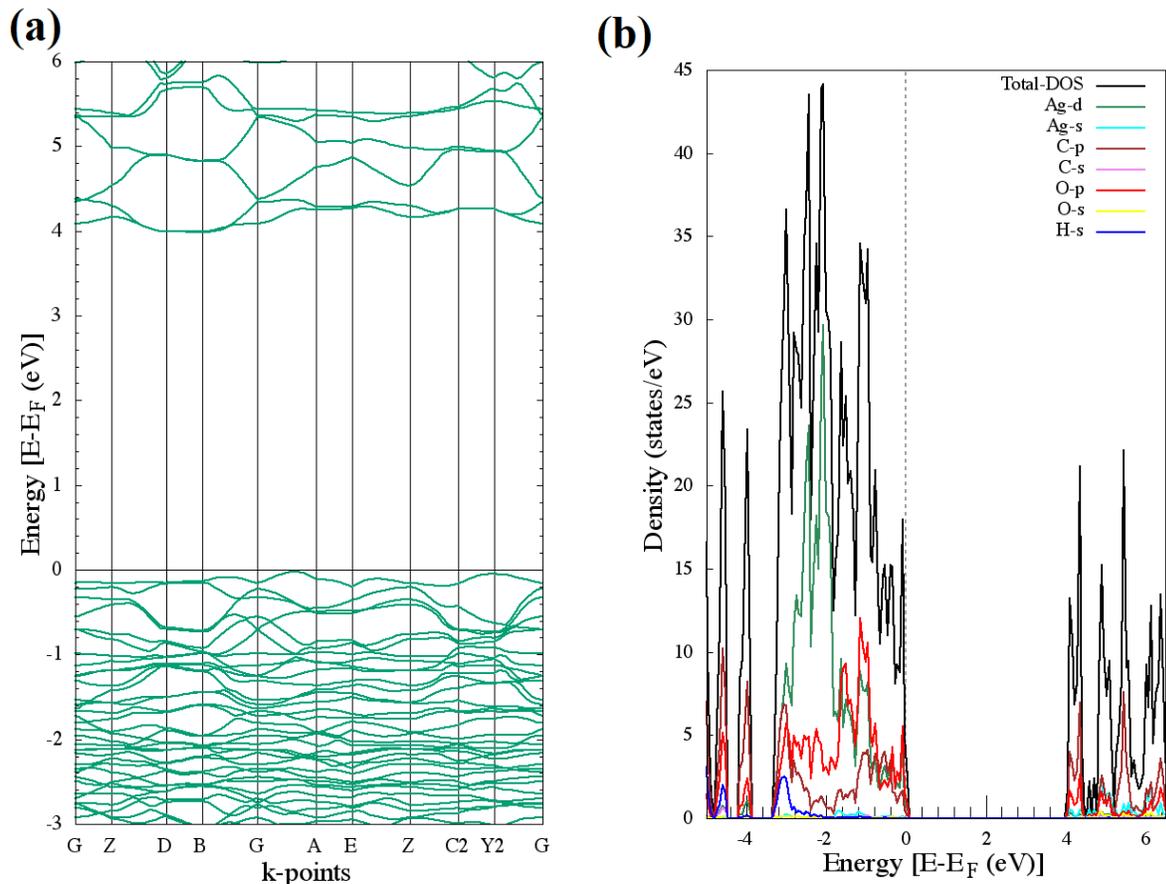
Figure 4. (a) Band structure, and (b) total density of states (black) and partial density of states (other colored area) of Ag(I)-CP using hybrid exchange-correlation HSE06.

268   In order to obtain a detailed electronic structure for Ag(I)-CP, the band structure and the

269   density of states (DOS) of the Ag(I)-CP were calculated using hybrid density functional theory

270   (HSE06), as implemented in the Vienna *Ab initio* Simulation Package (VASP). The band

271   structure (HSE06) calculated along high symmetry special *k*-points is shown in Figure 4a. Equal

272   energy valence band maxima (VBM) are located at Y2 and in between the Γ and A points. The

273   conduction band minima (CBM) are at B and D. This means that the smallest indirect band gap

274   (E_g) occurs with a calculated energy of 4.0 eV between VBM and CBM. However, the direct

275   band gap at B and D is only 0.1 eV greater at 4.1 eV. This small energy difference suggests that

276   the Ag(I)-CP would mostly behave as a direct band gap material giving it higher quantum

277   efficiency than would be expected for an indirect band gap material. The partial density of states

278   (p-DOS) over a broader energy range is given in Figure S5, this reveals that Ag 4d orbitals are

279   mostly confined between -4 to 0 eV (relative to the Fermi level), C 2s orbitals between -25 to -9

280   eV, while the 2s orbitals of O lie deep in the energy spectrum between -24 to -21 eV. The

281   valence band maxima (VBM) is composed of an admixture of Ag 4d and O 2p orbitals with

282   contribution from C 2p states (Figure 4b). On the other hand, the conduction band minima

283   (CBM) have a majority of 2p states of C with some contribution from the corresponding 2p

284   states of O (Figure 4b and Figure S5 and S6). Appearance of Ag *4d* and *5s* states at the CBM is

285   also observed (as shown in Figure S6) as would be expected from the hybridization of Ag 4d and

286   Ag 5s[39,40,41]enhanced by the short Ag-Ag contact (2.9 Å). However, the features for Ag 4d and

287   5s are less intense than those of C 2p. The electronic band structure obtained from the hybrid

288   functional indicates a direct band gap of 4.1 eV. Experimental diffuse reflectance spectroscopy

289   (DRS) was also used to estimate the band gap using the Kubelka-Munk plot approach. Figure 3a

290   (inset) shows that the plot of [F(R)hv]^2 *vs hv* for the Ag(I)-CP is nearly linear at the adsorption

291   edge, indicating a direct transition, and extrapolation to the *hv* axis gives a band gap estimate of

292   3.7 eV in close agreement with the band gap calculated from hybrid DFT. The band gap of 2.3

293   eV obtained from PBE functional calculations (Figure S7a) differs from the experimental value

294   due to the well-known underestimation of the band gap in GGA-DFT, however the composition

295   (Figure S7b) of the calculated hybridized states of orbitals in the valance band and conduction

296   band, agrees well with the more accurate results obtained from the hybrid HSE06 method.[34]

297   The promising semiconducting properties of Ag(I)-CP prepared using the synthetic methods

298   described earlier led us to test the photocatalytic performance of the material using, firstly, a

299 photoelectrochemical approach. An anode containing the CP was prepared following the

300 procedure described in the methodology section. Figure 5a shows that, using the anode in an

301 electrochemical cell, a photocurrent response was observed which followed the on-off cycle of

302 illumination.
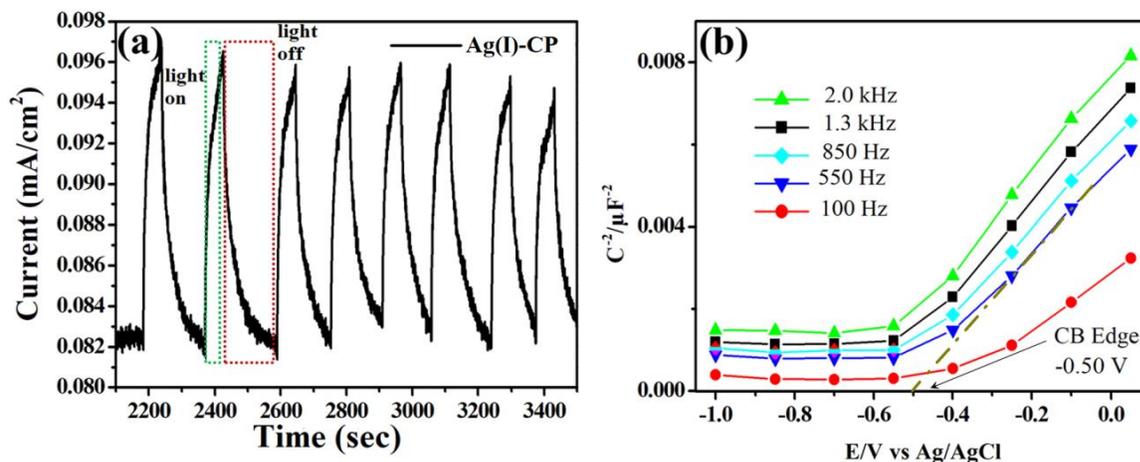
Figure 5. (a) Photocurrent response (300 W Xe lamps) of Ag(I)-CP in each on-off cycle, and (b) Mott-Schottky plots of Ag(I)-CP at different frequencies in 0.2 aq. Na_2SO_4 solutions (pH ~ 7).

303 This demonstrates that Ag(I)-CP is able to produce electron–hole pairs under light irradiation

304 (300 W Xenon lamps). In general, Xe lamp emits light less in the region of UV. However a

305 better photocurrent response could be achieved instead of Xe lamp if Hg lamp as light source

306 would have used. The Mott-Schottky plot of reciprocal squared cell capacitance C^{-2} *vs* applied

307 potential, *E* **(**Figure 5b**)** has a positive slope at all frequencies, which indicates that the as-

308 prepared sample behaves as a typical *n*-type semiconductor.[42] The flat-band potential of the

309 Ag(I)-CP is around -0.50 V *vs*. Ag/AgCl at pH 7, which is equivalent to -0.30 V *vs*. NHE at pH

310 7. The valance band potential of the Ag(I)-CP calculated from the optical band gap and the flat

311 band potential is +3.40 V *vs*. NHE at pH 7, which highlights the highly oxidative nature of the

312   material and suggests that Ag(I)-CP could find applications in challenging oxidation processes,

313   such as the removal of dye compounds from contaminated water.

314   The photocatalytic activity of the Ag(I)-CP was first assessed using the water splitting reaction

315   using irradiation with a 250W Hg lamp. The production of O_2 as a function of time using the

316   Ag(I)-CP as a photocatalyst was monitored by GC (Figure S8a). Background O_2 and N_2, which

317   were present at levels of a few hundred ppm in the reactor, could not be excluded; thus, initially

318   the O_2/N_2 volume ratio was considered for reliable qualitative understanding of O_2 generation.[43]

319   As shown in Figure S8a, this ratio consistently increased with irradiation time, implying that O_2

320   was produced by the photocatalytic reaction of water under light irradiation. Whereas when a

321   blank reaction (dark) was carried out, no change in the O_2/N_2 ratio was observed (Figure S8b).
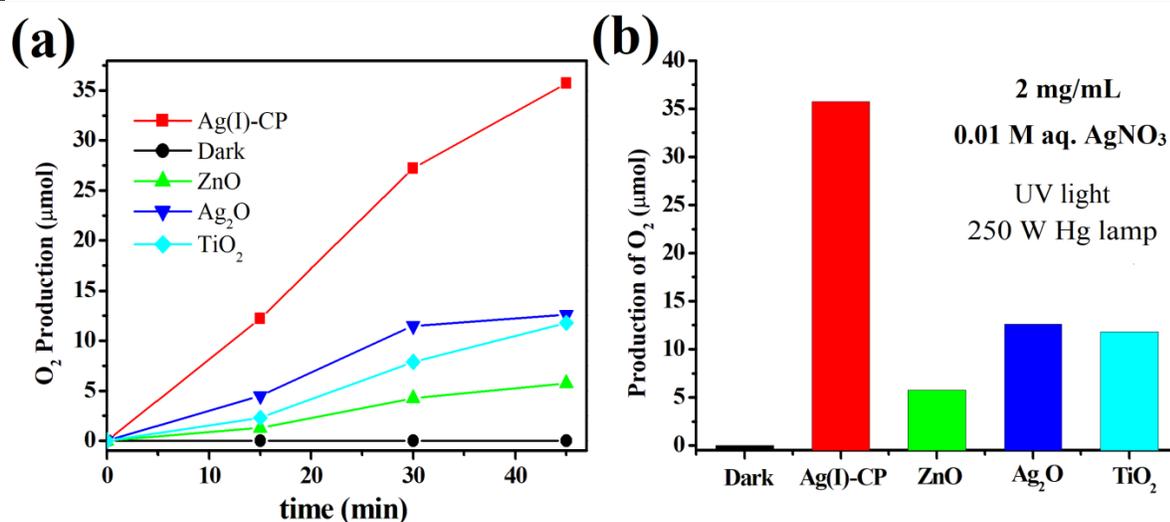
Figure 6. (a) Progress of photocatalytic O_2 evolution with respect to reaction time, and (b) a chart showing production of O_2 in dark and in presence of Ag(I)-CP, ZnO, Ag_2O, and TiO_2 under UV light (250 W Hg lamp) irradiation.

322   Further the quantitative estimation was done using calibration data in GC using mixture of

323   standard gases (O_2, N_2 and H_2) in TCD detector. Subtracting the background O_2, the amount of

O$_2$ produced in presence of Ag(I)-CP is estimated as shown in Figure 6a. 35 μmol of O$_2$ is produced within 45 minute of UV light irradiation and in compare to prepared Ag$_2$O, TiO$_2$, ZnO, Ag(I)-CP shows better performance in O$_2$ production efficiency.
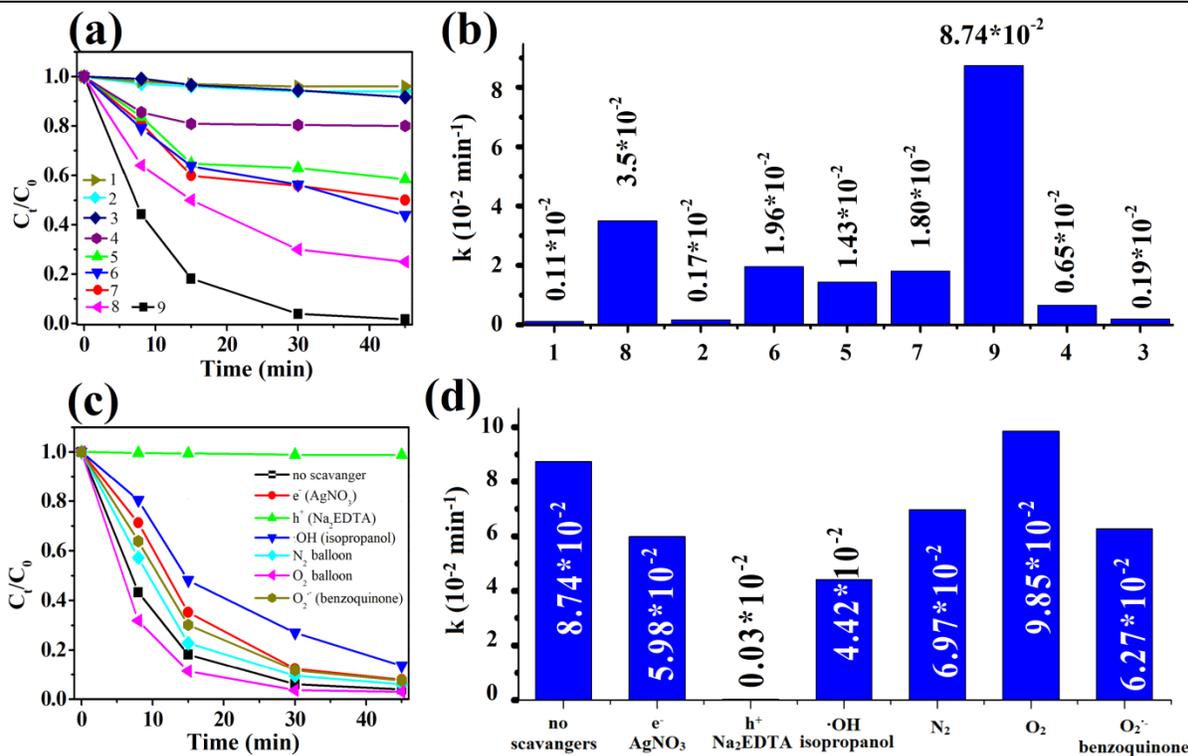
Figure 7. (a) Degradation plot (C$_t$/C$_0$ vs. time) of anionic tartrazine in presence of (1) (dark + Ag(I)-CP), (2) UV-Light (No catalyst), and (3) H$_2$bdc ligand, (4) AgNO$_3$ salt (0.05 mmol) (5) CuO, (6) TiO$_2$, (7) ZnO, (8) Ag$_2$O, and (9) Ag(I)-CP catalyst under irradiation of UV light (250 W Hg lamp), and (b) a chart showing their first-order rate constant value. (c) Effect of different quenchers and atmosphere on the photocatalytic degradation of tartrazine (C$_t$/C$_0$ vs. time) in presence of Ag(I)-CP, and (d) a chart showing their first-order rate constant value.

Notably, Ag(I)-CP shows 3 times better performance over Ag$_2$O (12 μmol), TiO$_2$ (11 μmol) and seven time better over ZnO (5 μmol) as presented in Figure 6b. To further test the oxidizing power of the photocatalytic system, we screen one model organic compounds: anionic tartrazine

19

330 azo dye (25 ppm) under UV irradiation (250 W Hg lamps). This represent important target

331 compound for removal by oxidation as its presence in water causes hazardous pollution in the

332 environment.[15,44,45] Before light irradiation, the reaction vessel containing (20 mL of 25 ppm)

333 tartrazine and prepared CP (1 mg/mL) was placed in the dark and stirred for 30 minute to

334 achieve adsorption-desorption equilibrium and Ag(I)-CP. Thereafter the light was turned on.

335 During the progress of the reaction, 3 mL aliquots were collected at regular time intervals

336 and centrifuged to remove the catalyst. The HPLC chromatogram (Figure S9) and UV-visible

337 spectra (Figure S9; inset) of the supernatant solution in the subsequent process shows a gradual

338 decrease of absorbance/peak area monitored at 428 nm indicative of dye degradation. Figure 7a

339 shows that almost full degradation of initial tartrazine takes place within 45 min using the

340 irradiated Ag(I)-CP as catalyst. An intermediate with mono substituted aromatic rings is obtained

341 during the degradation process and this was also monitored via absorption at 354 nm (Figure

342 S9).[45] Several intermediate molecules were identified by LC-MS and GC-MS during the

343 degradation process as depicted in Figure S11, and Figure S12. Further, ion chromatographic

344 and GC of the aqueous phase and gas phase reveals that the tartrazine is mineralizing into

345 CO_2, H_2O, SO_4^{2-}, and NH_4^+ in presence of the CP photocatalyst (Figure S14-Figure S15;

346 see supporting information Figure S13 for details of possible degradation pathways). To

347 confirm that Ag(I)-CP does act as a photocatalyst for this reaction several additional tests were

348 carried out and the results are included in Figure 7a. Firstly, tartrazine itself did not show self-

349 degradation upon irradiation by the same light source (see also Figure S10a). Secondly, no

350 tartrazine degradation is observed when Ag(I)-CP is included in the solution but without

351 illumination, so that Ag(I)-CP does not show catalytic performance in the absence of light. We

352 also found a very low rate of decomposition if the linker (ligand) alone was added to the

353 tartrazine solution (H$_2$bdc; $\sim$0.2$\times$10^{-2} min^{-1}). Similarly, use of a simple silver salt 0.05 mmol of

354 AgNO$_3$(*aq.*), gave only a very slow degradation rate (0.65$\times$10^{-2} min^{-1}) under the UV light,

355 revealing a small photosensitization effect. To compare with other common photocatalysts

356 Figure 7a also includes time online plots for the semiconducting materials mentioned in the

357 Methodology section. In addition the relative rates for these materials and for Ag(I)-CP are

358 compared in Figure 7b. The highest rate of degradation ($\sim$8.7$\times$10^{-2} min^{-1}) was observed when

359 Ag(I)-CP was employed as a photocatalyst, (Figure 7a, Figure 7b and Figure S10a). The

360 calculated rate is found to be more than twice that of Ag$_2$O ($\sim$3.5$\times$10^{-2} min^{-1}) and more than four

361 times greater than alternative semiconductors not based on silver: ZnO ($\sim$1.8$\times$10^{-2} min^{-1}), CuO

362 ($\sim$1.4$\times$10^{-2} min^{-1}), and TiO$_2$ ($\sim$1.9$\times$10^{-2} min^{-1}).

363 To check on the mode of operation of the Ag(I)-CP photocatalyst, a series of quenching

364 experiments were performed (Figure 7c). In the presence of a hole scavenger or with the

365 inclusion of $\cdot$OH scavengers significant decreases in the rate of tartrazine degradation

366 compared to the unmodified system were observed (rate = 3.0$\times$10^{-4} min^{-1} with Na$_2$EDTA as

367 hole scavenger and rate = 4.4$\times$10^{-2} min^{-1} with isopropanol as $\cdot$OH scavenger). This suggests that

368 photo generated h$^+$ and $\cdot$OH are the main active species that facilitate the tartrazine degradation

369 process. There were also slight decreases in the measured tartrazine degradation rates observed

370 in presence of AgNO$_3$ (e$^-$ scavengers, rate = 5.9$\times$10^{-2} min^{-1}), and benzoquinone BQ, (O$_2$$^-$

371 scavenger, rate = 6.2$\times$10^{-2} min^{-1}), respectively (see Figure 7c; Figure 7d and Figure S10b).

372 Hence, in addition to the main active species (h$^+$), electrons in the CBM (e$^-$) may also play a

373 secondary role. This may also explain why a slight reduction in the rate (6.9$\times$10^{-2} min^{-1}) was

374 observed under a N$_2$ atmosphere, whereas the rate of the reaction was accelerated under an O$_2$

375 atmosphere (rate = 9.8$\times$10^{-2} min^{-1}). Further, trapping experiments for hole and $\cdot$OH radical

376 were performed using TEMPO and coumarin as probes.[17,44,46] TEMPO is EPR active and

377 hence samples using this quenching agent were also characterized using EPR spectroscopy

378 (Figure 8a). The intensity of the signal corresponding to TEMPO was seen to gradually decrease

379 with exposure to UV light in the presence of Ag(I)-CP, which infers oxidation of the TEMPO

380 due to photo-generated holes.[17,46] The introduction of coumarin in another set of experiments

381 gave a gradual increase of fluorescence intensity (Figure 8b), which can be attributed to the

382 formation of ·OH adducts with the non-fluorescent coumarin molecules. This results in the

383 generation of a fluorescent 7-hydroxy coumarin[44] and so the fluorescence intensity is found to

384 increase gradually with respect to irradiation time due to the photocatalytic generation of ·OH

385 radicals.
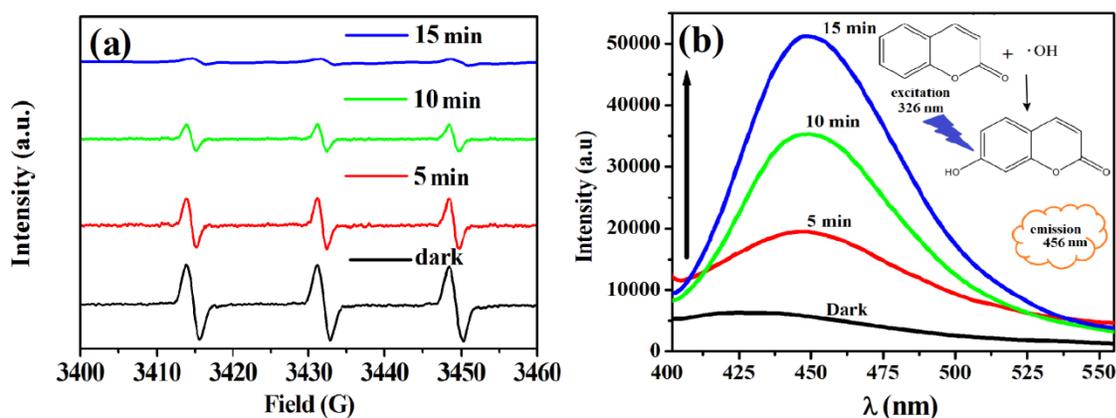
Figure 8. (a) Time dependent EPR spectra of TEMPO-h^+, and (d) fluorescence spectra of 7-hydroxy coumarin generated by ·OH radical adduct trapped by coumarin probe.

386 Hence, these quenching experiments confirm that the species mainly responsible for

387 photocatalytic degradation of tartrazine into mineralized products are h^+ and ·OH. CP is also a

388 promising material for the photo-oxidation of cationic RhB dye and chlorinated organic

389 pesticides. Figure S16 and Figure S17a show the time dependent HPLC chromatogram of 2,4-

390   DCP and absorption spectra of RhB, respectively. Within 45 min, 84% of RhB is oxidized, with

391   a calculated rate constant of 4.2×10^{-2} min^{-1}. About 78% of 2,4-DCP is dechlorinated within 45

392   min of starting the experiment, corresponding to a rate constant of 3.4×10^{-2} min^{-1} (Figure S17b

393   and Figure S17c).

394   In order to more fully understand the high photocatalytic activity of Ag(I)-CP, the

395   electronic density at the valance band and conduction band edges was also plotted to allow

396   discussion of the likely charge transfer process resulting from photoexcitation. It can be seen

397   from Figure 9a that electronic density near the VBM is located on the $4d$ orbitals of Ag$^+$ from the

398   metal site and the $2p$ orbitals of O atoms and aromatic C atom in the linker molecules. While the

399   electron density located at CBM is found on the carboxylate C atoms and on the C atoms in the

400   aromatic region of the linker. This demonstrates that there is obvious charge transfer from Ag-O

401   cluster from Ag$_2$O$_4$ unit of Ag$_2$O$_4$C$_8$H$_4$ species to π^* of the ligand giving an M $\rightarrow \pi^*$ transition,

402   *i.e.* MLCT.[47] However from Bader charges (shown in Table S1) for the atoms highlighted in the

403   structure (Figure S18) revealed the Ag atoms in the structure have calculated Bader charges

404   averaging $\sim$ +0.75e, confirming the formal oxidation state assignment of Ag$^+$. C1-C4

405   (carboxylate carbon atoms attached to phenyl rings) have charges of +1.51e to +1.53e due to the

406   strong bond polarization for C=O in carboxylate groups. Correspondingly, the charges calculated

407   for the carboxylate O atoms (O1-O8) average -1.12 e. Aromatic carbon atoms (C5-C16) bear

408   much lower charges (-0.06 to +0.15). Generally speaking, the more delocalized the electrons are

409   in the covalent bond, the more conducive it is for charge transfer,[48] hence C=C being more

410   covalent in character compared to C=O, Ag-O, favours LCCT $\pi \rightarrow \pi^*$ (process more efficiently

411   rather than MLCT. In addition, we cannot exclude a little contribution of hybridised Ag (d-s)

412   states at the CBM which resulted from M-M interaction, which includes a little admixture of

413 metal centre charge transfer as it was evident from luminescence behaviour of the CP (Figure

414 3b), however the majority of the CBM is formed by C *2p* states. The nature of the Ag–O

415 bonding, Ag-Ag interaction does not affect the characteristics of the CBM

416 significantly.[14,41,47]Hence, ligand centred charge transfer (LCCT) with admixture of MLCT

417 modified by *d-s* state in the CP resulted in a generation of electron and hole in the active site.

418 Further, the dispersive nature of the CBM, favors high mobility, allowing photo generated holes

419 to migrate away from their production sites, which is important to allow the efficient production

420 of free electrons and holes required for photo activity.
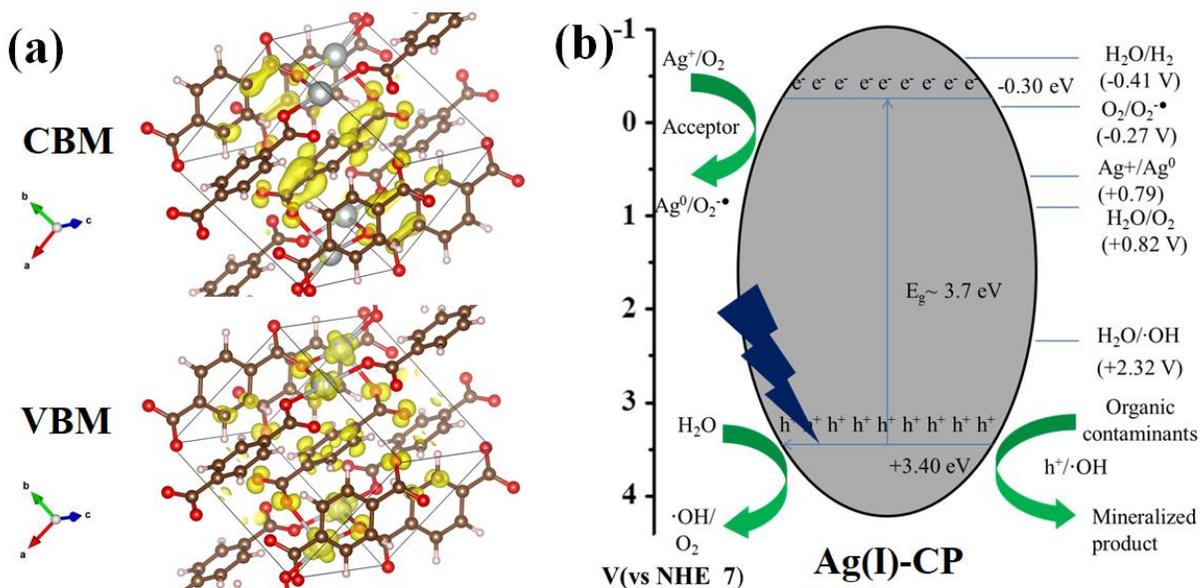
Figure 9. (a) Electron density at VBM (lower) and CBM (upper) of the Ag(I)-CP, and (b) UV light driven charge separation in the Ag(I)-CP and generated ROS responsible for OER and oxidation of model organic compounds such as tartrazine, RhB and 2,4 DCP.

421 Accordingly Ag(I)-CP is able to generate ROS (·OH) from an aqueous system, as holes (h^+)

422 generated in the VB have a potential (+3.40V *vs* NHE) below the reduction potential for

423 H_2O/·OH (+2.32V *vs* NHE at pH 7)[15,17]. This favours the production of oxidizing species

424   thermodynamically (Figure 9b). The position of the VBM edge of the CP (+3.40 V *vs* NHE is

425   deeper than VBM (< +3 V *vs* NHE) of other common semiconductor systems such as TiO_2[49],

426   ZnO[49], Ag_2O[44], and CuO[49]. Hence, this leads to the observed higher activity of Ag(I)-CP over

427   the more conventional metal oxides. Nevertheless, the CBM is not low enough to produce H_2

428   from H_2O (-0.42 V *vs* NHE at pH 7), but the production of $O_2^{\cdot-}$ from O_2 (-0.27 V *vs* NHE) is

429   favorable, because of thermodynamically permeable conduction band edge potential (-0.30 V *vs*

430   NHE) of the CP system.[50, 51, 52] As we have shown, the generated hole (h^+) and free hydroxyl

431   radicals from water/$O_2^{\cdot-}$ are able to oxidize organic compounds such as tartrazine, RhB and 2,4-

432   DCP to give mineralized products, following the steps (1-7) outlined below.

433    $\text{Ag(I)-CP} + h\nu \rightarrow \text{Ag(I)-CP}\,(h^+ + e^-)$ (1)

434    $\text{Ag(I)-CP(s)} \rightarrow \text{Ag(I)-CP (aq)} \rightarrow 2\text{Ag}^+\,(aq) + \text{bdc}^{2-}\,(aq)$ (2)

435    $\text{H}_2\text{O} + \text{Ag(I)-CP}\,(h^+) \rightarrow \cdot\text{OH} + \text{H}^+$ (3)

436    $\text{OH}\cdot + \text{Pollutants} \rightarrow \text{Degraded products} \rightarrow \text{CO}_2\,(g)\uparrow + \text{H}_2\text{O}$ (4)

437    $\text{Ag(I)-CP}\,(h^+) + \text{Pollutants} \rightarrow \text{Degraded products} \rightarrow \text{CO}_2\,(g)\uparrow + \text{H}_2\text{O}$ (5)

438    $\text{Ag(I)-CP}\,(e^-) + \text{Ag}^+\,(aq) \rightarrow \text{Ag}^0\,(s)$ (6)

439    $\text{O}_2(g) + \text{Ag(I)-CP}(e^-) \rightarrow \text{O}_2^{\cdot-} + 2\text{H}^+ + 2e^- \rightarrow \text{H}_2\text{O}_2 + e^- \rightarrow \cdot\text{OH} + {}^-\text{OH}$ (7)
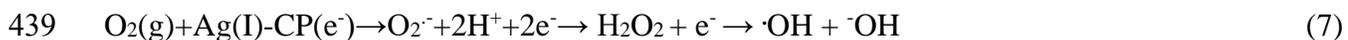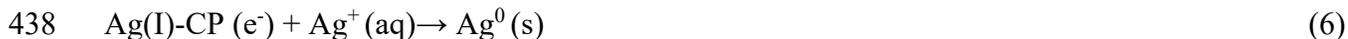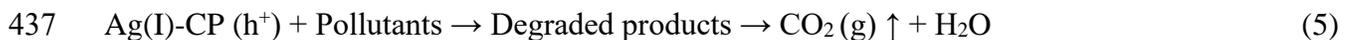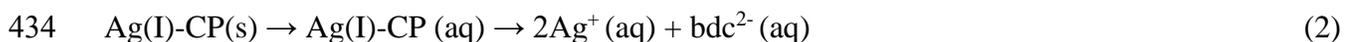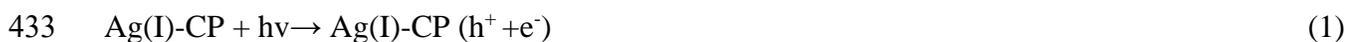
440

441   CP could be recycled and gives a photocatalytic efficiency of 93% in the 4th cycle (Figure 10a)

442   for the photocatalytic oxidation of tartrazine. A little admixture of Ag *s* state hybridized with Ag

443   *d* state in the CBM favours the reduction of lattice Ag^+ as observed in XPS (Figure 10b) and

444   XRD pattern (Figure 10c) of used CP after photocatalysis.
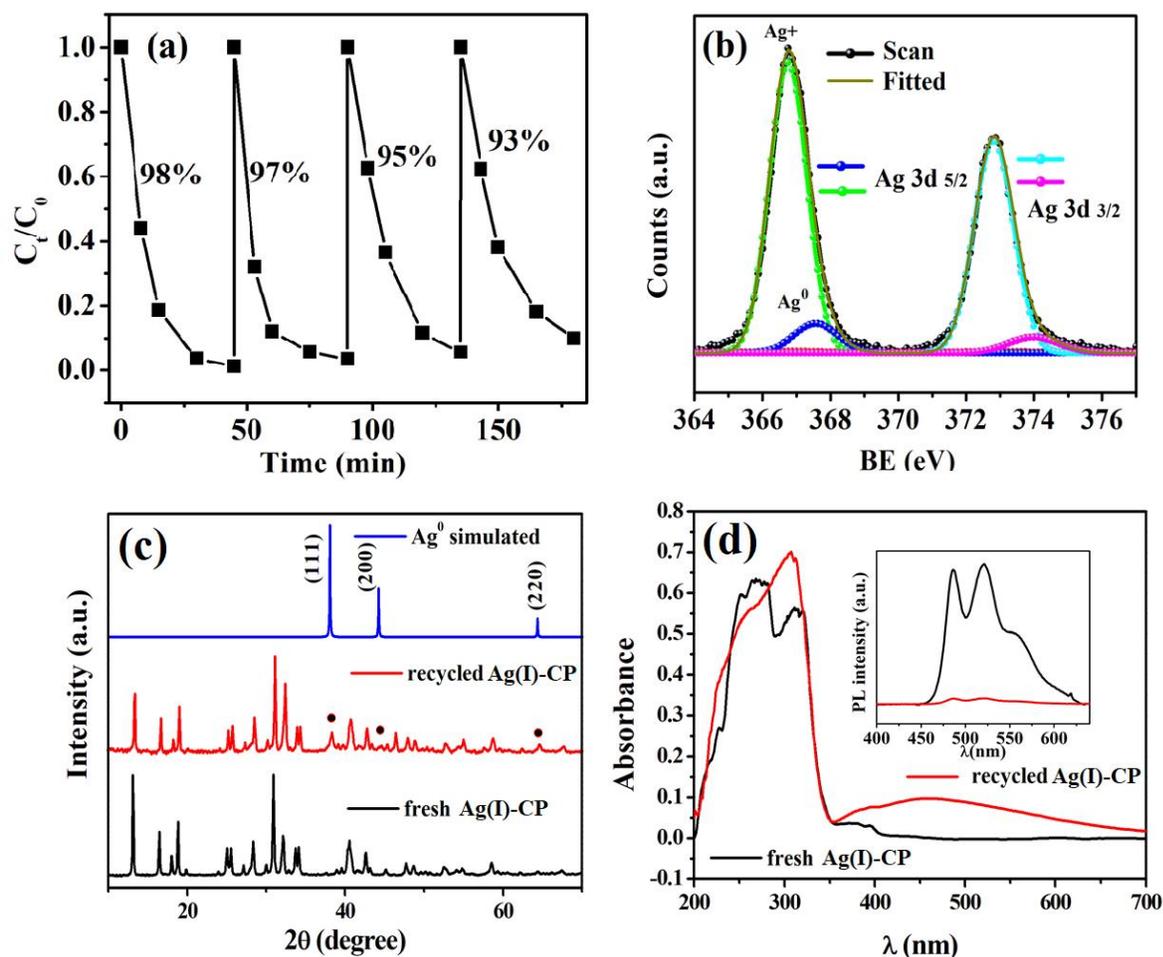
Figure 10. (a) Recyclability test of the Ag(I)-CP for the degradation of 25 ppm tartrazine under UV light irradiation for 4th cycle. (b) Ag 3*d* XPS spectra of used Ag(I)-CP photocatalyst. (c) PXRD patterns of the used (after 4th cycle) Ag(I)-CP and fresh Ag(I)-CP. (d) DRS spectra, and PL spectra (inset) of the used (after 4th cycle) and fresh Ag(I)-CP.

445   However, the states at the CBM are predominantly the π* orbitals of the organic linker and

446   therefore, the reduction of atmospheric oxygen is preferred. Hence, the Ag(I)-CP exhibits less

447   photo corrosion than other Ag based semiconducting systems as we have found the content of

448   Ag[0] estimated by deconvolution of Ag 3*d* peak in XPS from this used Ag(I)-CP material is only

449   5.8 atomic% (Figure 10b, Figure S17d and Table S2). XRD analysis (Figure 10c) shows that the

450   photocatalysts even after the 4th cycle also retain its original Ag(I)-CP structure with a weak

451   diffraction pattern corresponding to Ag^0. Figure 10d depict the comparison of DRS spectra of

452   fresh and used Ag(I)-CP samples. Noticeably, the small percentage of Ag^0 deposited due to

453   photo reduction of the Ag(I)-CP shows as a SPR band at around 440 nm (DRS spectra: Figure

454   10d), which disfavors the recombination process (PL spectra: Figure 10d; inset) shifts the light

455   harvesting efficiency from UV to UV-Visible light.[13] Obviously, Ag(I)-CP is expected serve as a

456   photocatalyst for oxidation of tartrazine in presence of simulated sunlight. Comparative studies

457   on oxidation of tartrazine by Ag(I)-CP catalyst were carried out under different light irradiation

458   conditions (refer Figure S19), such as UV light (250 W Hg lamp), simulated sunlight (250 W

459   sun-photo lamp), and visible light (250 W tungsten lamp, λ≥420 nm). Since, the tartrazine itself

460   absorbs light at λ_{max} = 428 nm and it could assist photocatalysis through self-sensitization

461   process. However, the tartrazine degradation by our catalyst was minimum (~ 20%) under the

462   visible light (shown in Figure S19). Overwhelmingly, the degradation efficiency of tartrazine by

463   Ag(I)-CP was maximum (~ 98%) under the UV light irradiation. On contrary to the visible light,

464   in presence of simulated sunlight the degradation efficiency of the dye had increased to moderate

465   level (~ 42%), which is attributed by the combined effect of photocatalytic activity of Ag(I) CP

466   (in UV light region) along with photo-sensitization of the dye (in visible region). Hence,

467   combination of Ag(I)-CP with other semi-conductive/metal doped materials or organic

468   sensitizers (in optimized composition) could serve as efficient visible light/sun light active

469   photocatalytic systems, which will be a progressive research-topic investigated in near future.

470

471   **CONCLUSIONS**

472   In summary, we have presented nano-micro structured Ag(I)-CP as LCCT accompanied with

473   MLCT based photocatalytic materials. Theoretical (hybrid DFT) and experimental evidence

474   from DRS, PL and photoelectrochemical experiments support the behavior of Ag(I)-CP as new

475   class of light active semiconductor. Ag(I)-CP was found to exhibit OER activity under UV light

476   resulting from active hole generation from light induced charge separation. The material was

477   successfully applied as a catalyst for the elimination of organic pollutants in aqueous solution.

478   Ag(I)-CP could be readily recycled, maintaining high activity after four successive uses as a

479   photocatalyst. The photocatalytic activity originates from the valance band position (hole) and

480   conduction band position (e$^-$) of the material, which are capable of directly activating organic

481   substrates via photogenerated h$^+$ or activating water and atmospheric oxygen, prompting

482   oxidative elimination of the model compounds using $\cdot$OH radical species. In future, the

483   morphology and band energy of the photocatalytic system (the CP exploited in this work) could

484   be further engineered by tuning linker ligands or incorporating different metals in order to gain

485   higher photoactivities for executing wide varieties of photocatalytic/photo-redox reactions.

486

487   **ASSOCIATED CONTENT**

488   The following files are available free of charge.

489

490   FTIR spectra, Comparison of XRD pattern with Ag and Ag$_2$O, 2D and 3D packing structure, and

491   asymmetric unit present in the Ag(I) coordination polymer, XRD pattern of prepared metal

492   oxide, N$_2$ adsorption-desorption isotherm, Electronic density of states (DOS/pDOS), Band

493   structure (GGA-PBE& HSE06) of the CP. GC chromatogram for water oxidation and HPLC,

494 UV-vis absorption spectra, LCMS, GC for CO_2, GC-MS, Ion chromatograph for the degradation

495 of tartrazine and first order kinetics plot. UV-visible absorption spectra of rhodamine B, HPLC

496 of 2, 4 DCP, and kinetics plots for respective degradation. XPS spectra of the CP after used and

497 Table of percentage of Ag^0 present in the Ag(I) coordination polymer. Table of Bader charges of

498 the atom present in the coordination polymer.

499 **AUTHOR INFORMATION**

500 **Corresponding Author**

501 *Dr. Rajakumar Ananthakrishnan,*
502 *Department of Chemistry, Environmental Materials & Analytical Chemistry Laboratory, Indian*
503 *Institute of Technology, Kharagpur 721302, India*
504 *E-mail: raja.iitchem@yahoo.com; Fax: +91 3222-282252; Tel: +91 3222 282322*
505

506 **Notes**

507 The authors declare no competing financial interest.

518 ABBREVIATIONS

519 CP coordination polymer; ROS reactive oxygen species; RhB rhodamine B; 2, 4 DCP 2, 4

520 dichlorophenol; bdc^{2-} benzene dicarboxylate.

521 **REFERENCES**

522 1) Chang, K.; Li, M.; Wang, T.; Ouyang, S.; Li, P.; Liu, L.; Ye, J. Drastic

523 Layer-Number-Dependent Activity Enhancement in Photocatalytic H_2 Evolution

524 over nMoS$_2$/CdS ($n \geq 1$) Under Visible Light. *Adv. Energy Mater.* **2015**, *5*, 1402279.

525 2) Linsebigler, A. L.; Lu, G.; Yates, J. T. Photocatalysis on TiO$_2$ Surfaces: Principles,

526 Mechanisms, and Selected Results. *Chem. Rev.* **1995**, *95*, 735-758.

527 3) Dhakshinamoorthy, A.; Asiri, M. A.; Garcia, H. Metal–Organic Framework (MOF)

528 Compounds: Photocatalysts for Redox Reactions and Solar Fuel Production. *Angew.*

529 *Chem. Int. Ed.* **2016**, *55*, 5414-5445.

530 4) O'Keeffe, M.; Yaghi, O. M. Deconstructing the Crystal Structures of Metal–Organic

531 Frameworks and Related Materials into Their Underlying Nets. *Chem. Rev.* **2011**, *112*,

532 675-702.

533 5) Nasalevich, M. A.; Van der Veen, M.; Kapteijn, F.; Gascon, J. Metal–Organic

534 Frameworks as Heterogeneous Photocatalysts: Advantages and Challenges.

535 *CrystEngComm* **2014**, *16*, 4919-4926.

536 6) Alvaro, M.; Carbonell, E.; Ferrer, F. B.; Xamena, F. X. L.; Garcia, H. Semiconductor

537 Behavior of a Metal-Organic Framework (MOF). *Chem. Eur. J.* **2007**, *13*, 5106-5112.

538   7) Dan-Hardi, M.; Serre, C.; Frot, T.; Rozes, L.; Maurin, J.; Sanchez, C.; Fe´rey, J. A New

539   Photoactive Crystalline Highly Porous Titanium(IV) Dicarboxylate. *J. Am. Chem. Soc.*

540   **2009**, *131*, 10857-10859.

541   8) Hendon, C. H.; Tiana, D.; Fontecave, M.; Sanchez, C.; D'arras, L.; Sassoye, C.; Rozes,

542   L.; Mellot-Draznieks, C.; Walsh, A. Engineering the Optical Response of the Titanium-

543   MIL-125 Metal–Organic Framework through Ligand Functionalization. *J. Am. Chem.*

544   *Soc.* **2013**, *135*, 10942-10945.

545   9) Wu, X. P.; Gagliardi, L.; Truhlar, D. G. Cerium Metal-Organic Framework for

546   Photocatalysis. *J. Am. Chem. Soc.* **2018**, *140*, 7904-7912.

547   10) Ji, M.; Lan, X.; Han, J.; Hao, C.; Qiu, J. Luminescent Properties of Metal–Organic

548   Framework MOF-5: Relativistic Time-Dependent Density Functional Theory

549   Investigations. *Inorg. Chem.* **2012**, *51*, 12389-12394.

550   11) Muhammad, U.; Shruti, M.; Kuang-Lieh, L. Semiconductor Metal–Organic

551   Frameworks: Future Low-Bandgap Materials. *Adv. Mater.* **2017**, *29*, 1605071-1605075.

552   12) Gong, Y.; Shi, H. F.; Jiang, P. G.; Hua, W.; Lin, J. H. Metal(II)-Induced Coordination

553   Polymer Based on 4‑(5-(Pyridin-4-yl)-4H-1,2,4-triazol-3-yl)benzoate as an

554   Electrocatalyst for Water Splitting. *Cryst. Growth Des.* **2014**, *14*, 649-657.

555   13) Wang, F.; Li, F. L.; Xu, M. M.; Yu, H.; Zhang, J. G.; Xia, H. T.; Lang, J. P. Facile

556   Synthesis of a Ag(I)-doped Coordination Polymer with Enhanced Catalytic

557   Performance in the Photodegradation of Azo Dyes in Water. *J. Mater. Chem. A* **2015**,

558   *3*, 5908-5916.

559   14) Martin, D. J.; Liu, G.; Moniz, S. J. A.; Bi, Y.; Beale, A. M.; Ye, J.; Tang, J. Efficient

560   Visible Driven Photocatalyst, Silver Phosphate: Performance, Understanding and

561   Perspective. *Chem. Soc. Rev.* **2015**, *44*, 7808-7828.

562   15) Jianting, T.; Yonghong, L.; Haizhu, L.; Zhen, T.; Datang, L. A Novel

563   Ag_3AsO_4 Visible-Light-Responsive Photocatalyst: Facile Synthesis and Exceptional

564   Photocatalytic Performance. *Chem. Commun.* **2013**, *49*, 5498-5500.

565   16) Zheng, C.; Yang, H. Assembly of Ag_3PO_4 Nanoparticles on Rose Flower-like Bi_2WO_6

566   Hierarchical Architectures for Achieving High Photocatalytic Performance. *J. Mater.*

567   *Sci.: Mater. Electron.* **2018**, *29*, 9291.

568   17) Mandal, S.; Ananthakrishnan, R. Sustainable Design of Hierarchically Porous

569   Ag_3PO_4 Microspheres through a Novel Natural Template and Their Superior

570   Photooxidative Capacity. *ACS Sustainable Chem. Eng.* **2018**, *6*, 1091-1104.

571   18) Wang, X.; Li, S.; Yu, H.; Yu, J.; Liu, S. Ag_2O as a New Visible-Light Photocatalyst:

572   Self-Stability and High Photocatalytic Activity. *Chem. Eur. J.* **2011**, *17*, 7777-7780.

573   19) Yoshida, R.; Suzuki, Y.; Yoshikawa. S. Syntheses of TiO_2(B) Nanowires and TiO_2

574   Anatase Nanowires by Hydrothermal and Post-Heat Treatments. *J. Solid State Chem.*

575   **2005**, *178*, 2179-2185.

576   20) Georgekutty, R.; Seery, M. K.; Pillai, S. C. A Highly Efficient Ag-ZnO Photocatalyst:

577   Synthesis, Properties, and Mechanism. *J. Phys. Chem. C* **2008**, *112*, 13563-13570.

578   21) Kresse, G.; Furthmüller, J. Efficient Iterative Schemes for *Ab-initio* Total-Energy

579   Calculations Using a Plane-Wave Basis Set. *Phys. Rev. B* **1996**, *54*, 11169-11186.

580 22) Kresse, G.; Furthmüller, J. Efficiency of *Ab-initio* Total Energy Calculations for

581   Metals and Semiconductors Using a Plane-Wave Basis Set. *Comput. Mater. Sci.* **1996**,

582   *6*, 15-50.

583 23) Blöchl, P. E. Projector Augmented-Wave Method. *Phys. Rev. B* **1994**, *50*, 17953-

584   17979.

585 24) Perdew, J. P.; Burke, K.; Ernzerhof, M. Generalized Gradient Approximation Made

586   Simple. *Phys. Rev. Lett.* **1996**, 77, 3865-3868.

587 25) Heyd, J.; Scuseria, G. E. Hybrid Functionals Based on a Screened Coulomb potential.

588   *J. Chem. Phys.* **2003**, *118*, 8207-8215.

589 26) Heyd, J.; Scuseria, G. E.; Ernzerhof, M. Erratum: "Hybrid Functionals Based on a

590   Screened Coulomb Potential. *J. Chem. Phys.* **2006**, *124*, 219906.

591 27) Monkhorst, H. J.; Pack, J. D. Special Points for Brillouin-Zone Integrations. *Phys. Rev.*

592   *B* **1976**, *13*, 5188-5192.

593 28) Hinuma, Y.; Pizzi, G.; Kumagai, Y.; Oba, F.; Tanaka, I. Band Structure Diagram Paths

594   Based on Crystallography. *Comp. Mat. Sci.* **2017**, *128*, 140-184.

595 29) Bader, R. F. W. Atoms in Molecules: A Quantum Theory, Clarendon Press, Oxford,

596   **1990**.

597 30) Henkelman, G.; Arnaldsson, A.; Jo´nsson, H. A Fast and Robust Algorithm for Bader

598   Decomposition of Charge Density. *Comput. Mater. Sci.* **2006**, *36*, 354-360.

599   31) Guerra, C. F.; Handgraaf, J. W.; Baerends, E. J.; Bickelhaupt, F. M. Voronoi
600   Deformation Density (VDD) Charges: Assessment of the Mulliken, Bader, Hirshfeld,
601   Weinhold, and VDD methods for Charge Analysis. *J. Comput. Chem.* **2004**, *25*, 189-
602   210.

603   32) Wang, G.; Liu, Y.; Huang, B.; Qin, X.; Zhang, X.; Dai, Y. A Novel Metal–Organic
604   Framework Based on Bismuth and Trimesic Acid: Synthesis, Structure and Properties.
605   *Dalton Trans*. **2015**, *44*, 16238-16241.

606   33) Sun, D.; Cao, R.; Bi, W.; Weng, J.; Hong, M.; Liang, Y. Syntheses and
607   Characterizations of a Series of Silver-Carboxylate Polymers. *Inorg. Chim. Acta*. **2004**,
608   *357*, 991-1001.

609   34) Jiang, H.; Zhou, P.; Wang, Y.; Duan, R.; Chen, C.; Song, W.; Zhao, J. Copper-Based
610   Coordination Polymer Nanostructure for Visible Light Photocatalysis. *Adv. Mater.*
611   **2016**, *28*, 9776-9781.

612   35) Wu, Y.; Luo, H.; Wang, H. Synthesis of Iron(III)-Based Metal–Organic
613   Framework/Graphene Oxide Composites with Increased Photocatalytic Performance
614   for Dye Degradation. *RSC Adv.* **2014**, *4*, 40435-40438.

615   36) Ma, J. F.; Jin, Y.; Shun-Li, L.; Shu-Yan, S.; Hong-Jie, Z.; Hai-Shui, W.; Kui-Yue, Y.
616   Two Coordination Polymers of Ag(I) with 5-Sulfosalicylic Acid. *Cryst. Growth Des.*
617   **2005**, *5*, 807-812.

618   37) Allendorf, M. D.; Bauer, C. A.; Bhaktaa, R. K.; Houka. R. J. T. Luminescent Metal–
619   Organic Frameworks. *Chem. Soc. Rev.* **2009**, *38*, 1330-1352.

620   38) Han, L.; Yuan, D. K.; Wu, B. L.; Liu, C. P.; Hong, M. C. Syntheses, Structures and
621   Properties of Three Novel Coordination Polymers with a Flexible Asymmetrical
622   Bridging Ligand. *Inorg. Chim. Acta* **2006**, *359*, 2232-2240.

623   39) Sciau, P.; Kania, A.; Dkhil, B.; Suard, E.; Ratuszna, A. Structural Investigation of
624        $AgNbO_3$ Phases Using X-ray and Neutron Diffraction. *J. Phys. Condens. Matter*. **2004**,
625   *16*, 2795-2810.

626   40) Abrahams, S.; Bernstein, J. Crystal Structure of Piezoelectric Nonlinear-Optic
627        $AgGaS_2$. *J. Chem. Phys.* **1973**, *59*, 1625-1629.

628   41) Umezawa, N.; Shuxin, O.; Ye, J. Theoretical Study of High Photocatalytic
629   Performance of Ag_3PO_4. *Phys. Rev. B* **2011**, *83*, 0352021-0352028.

630   42) Gelderman, K.; Lee, L.; Donne, S. W. Flat-Band Potential of a Semiconductor: Using
631   the Mott–Schottky Equation. *J. Chem. Educ.* **2007**, *84*, 685-688.

632   43) He, Z. Q.; Wang, D.; Fang, H. Y.; Chen, J. M.; Song, S. Highly Efficient and Stable
633        $Ag/AgIO_3$ Particles for Photocatalytic Reduction of CO_2 under Visible Light.
634   *Nanoscale* **2014**, *6*, 10540-10544.

635   44) Yu, C.; Li, G.; Kumar, S.; Yang, K.; Jin, R. Phase Transformation Synthesis of Novel
636   Ag_2O/Ag_2CO_3 Heterostructure with High Visible Light Efficiency in Photocatalytic
637   Degradation of Pollutants. *Adv. Mater.* **2014**, 26, 892-898.

638   45) Al-Dawery, S. K. Photocatalyst Degradation of Tartrazine Compound in Waste Water
639   using TiO_2 and UV Light. *J. Eng. Sci. Technol*. **2013**, *8*, 683-691.

640   46) Rodr´iguez, N. A.; Parraab, R.; Grela, M. A. Structural Characterization, Optical

641   Properties and Photocatalytic Activity of MOF-5 and Its Hydrolysis Products:

642   Implications on Their Excitation Mechanism. *RSC Adv*. **2015**, *5*, 73112-73118.

643   47) Yanga, X.; Yan, D. Long-After Glow Metal–Organic Frameworks: Reversible Guest-

644   Induced Phosphorescence Tunability. *Chem. Sci.* **2016**, *7*, 4519-4526.

645   48) Wang, G.; Sun, Q.; Liu, Y.; Huang, B.; Dai, Y.; Zhang, X.; Qin, X. A Bismuth-Based

646   Metal–Organic Framework as an Efficient Visible-Light-Driven Photocatalyst. *Chem.*

647   *Eur. J.* **2015**, *21*, 2364-2367.

648   49) Haque, F.; Daenekel, T.; Kalantar-zadeh, K.; Oul, J. Z. Two-Dimensional Transition

649   Metal Oxide and Chalcogenide-Based Photocatalysts. *Nano-Micro Lett.* **2018**, *10*, 1-27.

650   50) Wood, P. M. The Redox Potential of the System Oxygen-Superoxide. *FEBS Lett.*

651   **1974**, *44*, 22-24.

652   51) Miyauchi, M.; Nakajima, A.; Watanabe, T.; Hashimoto, K. Photocatalysis and

653   Photoinduced Hydrophilicity of Various Metal Oxide Thin Films. *Chem. Mater.* **2002**,

654   *14*, 2812-2816.

655   52) Li, X.; Yu, J.; Jaroniec, M. Hierarchical Photocatalysts. *Chem. Soc. Rev.* **2016**, *45*,

656   2603-2636.

657

658

659

660   **TOC Graphic**

661